The electronic structure of $ZrSe_2$ and Cs_xZrSe_2 studied by angle-resolved photoelectron spectroscopy

1995 J. Phys.: Condens. Matter 7 7741

(http://iopscience.iop.org/0953-8984/7/40/006)

J. Phys.: Condens. Matter 6 (1995) 7741–7760. Printed in the UK

The electronic structure of $ZrSe_2$ and Cs_xZrSe_2 studied by angle-resolved photoelectron spectroscopy

H E Brauer†, H I Starnberg†, L J Holleboom‡ and H P Hughes§

† Department of Physics, Chalmers University of Technology and Göteborg University, S-412 96 Göteborg, Sweden

‡ Department of Theoretical Physics, University of Lund, S-223 62 Lund, Sweden

§ Cavendish Laboratory, Madingley Road, Cambridge CB3 0HE, UK

Received 3 July 1995

Abstract. We report an angle-resolved photoelectron spectroscopy study of the layered semiconductor $ZrSe_2$, and of changes in its electronic structure induced by *in situ* intercalation with Cs. The results show that the valence band structure of $ZrSe_2$ is initially of 3D character, but is transformed to become essentially 2D upon Cs intercalation. The observed changes are supported by self-consistent LAPW band calculations, and are not compatible with the rigid-band model. Changes in the Se 3d core level lineshape are attributed to an intercalation-induced increase in the carrier density in the lowest conduction band, which produces a different screening of the core hole.

1. Introduction

The compound $ZrSe_2$ belongs to the group of layered transition metal dichalcogenides (TMDCs), which are sometimes referred to as 'two dimensional' (2D). This description is not fully appropriate, and despite the fact that these materials do have highly anisotropic properties, there are several cases where the valence band dispersion perpendicular to the layers is comparable to the parallel dispersion [1–3].

One interesting property of these materials is the formation of intercalation complexes with foreign atoms or molecules between the layers [4–5]. The intercalation process is often interpreted within the rigid-band model, which can be a useful approximation for reaching a qualitative understanding of changes induced by the intercalation. The rigid-band model assumes that the host band structure remains unchanged upon intercalation, with only the band filling being altered by charge transfer from the intercalant to the host layers. Many of the observed changes can be explained in terms of such charge transfer, which is also considered to drive the energetics of the intercalation process. However, as intercalation of species larger than the available interstitial sites necessitates an increase of the interlayer separation, the degree of anisotropy is likely to be affected, producing changes not compatible with the rigid-band model.

In recent years, a method suitable for producing high-quality surfaces of intercalates under UHV conditions has received growing interest. In this method the intercalant is deposited *in situ* on the TMDC surface, from where it spontaneously intercalates. Of the monatomic species, the alkali metals have received most attention, since they have a strong tendency to donate their single valence electron to the host lattice, which limits the hybridization between the alkali metal and host valence bands. Of the alkali metals, Cs

0953-8984/95/407741+20$19.50

is an interesting choice since it has the largest ionic radius (1.69 Å) [6], and therefore the interlayer separation must by necessity increase significantly [7, 8]. Only a limited number of photoemission studies of *in situ* intercalated alkali metal/TMDC systems have been reported in the literature despite these promising opportunities [3, 9–18].

$ZrSe_2$ crystallizes with the 1T–CdI_2 structure, which is characterized by octahedrally coordinated metal atoms and layers stacked without lateral displacement. The six valence bands are primarily derived from Se 4p orbitals while the conduction bands are derived mainly from the Zr 4d orbitals. The valence band can hold 12 electrons per unit cell, so after filling the valence band, no electrons remain to occupy the conduction band. $ZrSe_2$ is therefore a semiconductor and has a band gap $E_g \sim 1$ eV, but since it cannot be grown with exact stoichiometry, some small amount of excess metal is always present and produces degenerate extrinsic properties. The extra electrons occupy the lowest levels of the conduction band, located as small electron pockets at the zone edges (around the LML lines). The experimental band structure of $ZrSe_2$ has to our knowledge not been reported, but calculated band structures, with some substantial deviations, have been published [1, 19–21]. Shepherd and Williams have presented UPS data (not angle-resolved) [22], and Jellinek *et al* XPS data [23] of $ZrSe_2$, in fair agreement with our results.

We report the first angle-resolved photoemission results for $ZrSe_2$, using synchrotron radiation, before and after intercalation with Cs. The dimensionality and the dispersion of the valence bands are closely studied to detect intercalation-induced changes, and to check the validity of the rigid-band model. The analysis involves self-consistent band structure calculations for $ZrSe_2$ and for the hypothetical compound $CsZrSe_2$ using the linear augmented plane wave (LAPW) method. Changes in the lineshape of the Se 3d core level after intercalation are interpreted in terms of an increased free carrier density when charge is added to the conduction band, producing increased screening of the core level hole.

2. Experimental details

The photoemission spectra were measured at the MAX-lab national synchrotron radiation facility in Lund, Sweden. The beamline incorporates a toroidal grating monochromator with three interchangeable gratings which provided photons with energies in the range 10–200 eV and a modified VSW hemispherical electron energy analyser. The electron energy analyser had $\pm 2°$ angular acceptance and typically 0.1 eV energy resolution. The synchrotron radiation was incident at $\Psi = 45°$ and polarized in the plane of incidence. All measurements were made at room temperature.

The $ZrSe_2$ single crystal was attached to the sample holder by silver-filled epoxy resin. A clean mirror-like (0001) surface was obtained by cleavage *in situ*. The sample was azimuthally oriented by LEED in both the $\bar{\Gamma}\bar{K}$ and $\bar{\Gamma}\bar{M}$ azimuths. The inequivalent $\bar{\Gamma}\bar{M}$ and $\bar{\Gamma}\bar{M}'$ crystallographic directions were identified as described by Law *et al* [24]. Cs was deposited at room temperature from a carefully outgassed SAES getter source. The deposition of Cs and the intercalation process were monitored by recording Cs 4d core level spectra. Valence band spectra, Zr 4p and Se 3d core level spectra were also recorded for pure and for Cs-intercalated $ZrSe_2$.

The base pressure in the measurement chamber was 3.5×10^{-10} Torr. The SAES getter source was operated at a current of 5.8 A for three minutes. Cs started to evaporate about 45 s after the current was switched on. The pressure was less than 1.8×10^{-9} Torr during the evaporations. The deposited amount of Cs was estimated to be far more than required to obtain monolayer coverage. The clean (0001) surface of $ZrSe_2$ (as well as of other TMDCs) is known to be chemically inert due to the absence of dangling bonds, but even the Cs-dosed

surface turned out to be remarkably inert. Core level and valence band spectra indicated only moderate contamination of the surface even up to 15 h after the initial Cs deposition. This inertness is probably due to the fact that no metallic Cs overlayer is formed at room temperature.

3. Calculations

The calculated band structure of $ZrSe_2$ was obtained by applying the LAPW method within the local density approximation (LDA) of density functional theory (DFT). In the calculations 65 k points in the irreducible part of the Brillouin zone (BZ) were used and 400 LAPW basis functions. The parametrized [25] Ceperley–Alder [26] form of the exchange–correlation potential was used. The structural parameters used were 3.77 Å and 6.16 Å for the in-plane and interlayer lattice parameters respectively [27]. A well known shortcoming of band structure calculations using the LDA for the exchange and correlation potential from DFT is the tendency to underestimate band gaps when applied to semiconductors. When comparing with experimental data this can be compensated for by shifting the conduction bands relative to the valence bands until good agreement is obtained (as is done in section 5). The calculated $ZrSe_2$ bands are presented in figure 1(a), with E_F located at the valence band maximum. There is a gap of 7–8 eV between the valence band and the Se 4s bands (not shown) which are located some 13–14 eV below the Fermi level. The calculation predicts that the Se 4s bands should have a dispersion of almost 1.5 eV.

The band structure of Cs-intercalated $ZrSe_2$ was calculated for the hypothetical compound $CsZrSe_2$, where the intercalated Cs ions were assumed to occupy octahedral sites between the $ZrSe_2$ layers. The in-plane lattice parameter was decreased to 3.73 Å (as compared to 3.77 Å for $ZrSe_2$) which is the experimentally determined value for $LiZrSe_2$ [4, 5]. The interlayer lattice parameter was increased to 8.73 Å (as compared to 6.16 Å for $ZrSe_2$): this estimate was based on ionic radii considerations. The calculated $CsZrSe_2$ bands are presented in figure 1(b): E_F is now located in the half-filled lowest conduction band. The Se 4s bands (again not shown) are now about 8–9 eV below the valence band, and possibly with smaller dispersion than for pure $ZrSe_2$. In between the valence and the Se 4s bands are Cs 5p bands (also not shown), located some 3–4 eV below the valence band; the calculation predicts almost 2 eV dispersion of these bands.

4. Experimental results

4.1. $ZrSe_2$

The character of the $ZrSe_2$ valence band was probed using both normal emission energy distribution curves (EDCs) with different photon energies and EDCs at a fixed photon energy with varying polar angle θ. Normal emission EDCs for different photon energies, $h\nu$, provide information about the valence band dispersion along the ΓA symmetry direction (perpendicular to the $ZrSe_2$ layers), while EDCs recorded in the $\bar{\Gamma}\bar{K}$ and $\bar{\Gamma}\bar{M}$ azimuthal directions provide information about the parallel dispersion. Figure 2 presents normal emission EDCs with $h\nu$ in the range 18–46 eV. Most structures are seen to disperse as $h\nu$ is changed, which is clear evidence of the 3D character of the valence band. Weak features from higher-order grating diffraction can be seen at E_F in the spectra for $h\nu = 18$ eV (Se 3d, fourth order), $h\nu = 30$ eV (Zr 4p, second order) and below the valence band for $h\nu = 22$ eV (Zr 4p, second order) and 24 eV (Se 3d, third order) respectively. The 3D character is also supported by the band structure calculation in figure 1(a), where there is

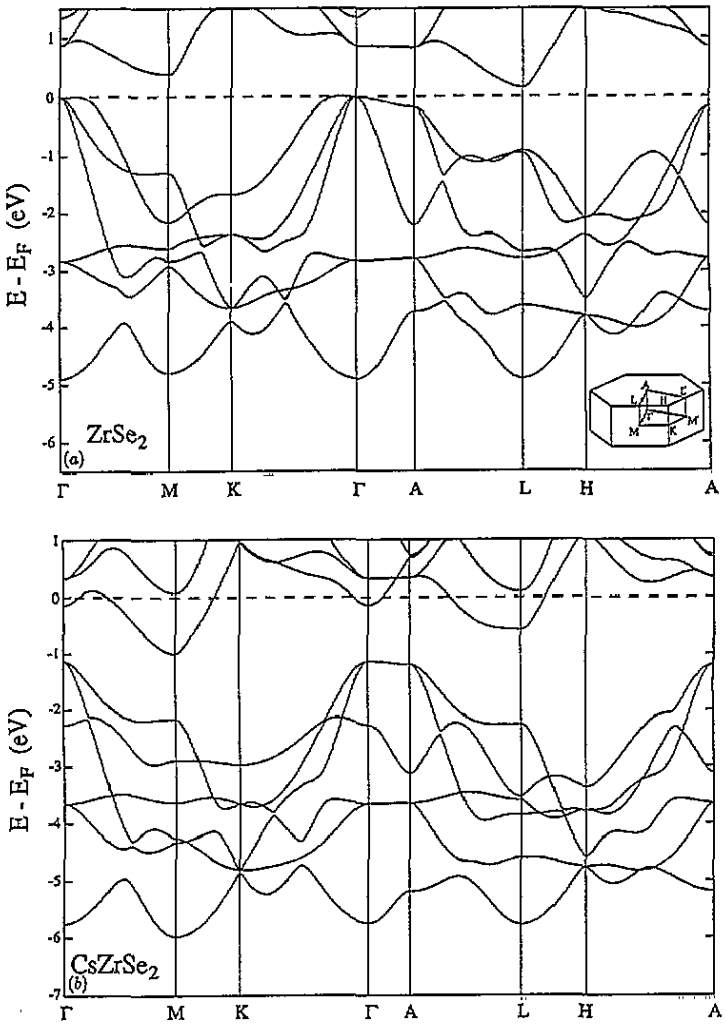

Figure 1. Calculated band structure using the LAPW method of (*a*) $ZrSe_2$ and (*b*) $CsZrSe_2$. The inset in (*a*) shows the hexagonal BZ with symmetry points.

one band with about 2 eV and one with over 1 eV dispersion between Γ and A. The flat top of the valence band and the almost dispersionless band at 4 eV binding energy (BE) are also consistent with the calculation.

EDCs recorded with $h\nu = 24$ eV in the $\bar{\Gamma}\bar{K}$ azimuthal direction are presented in figure 3. The polar angle θ ranges from $-16.5°$ to 53.5°; it should be noted that at high angles of emission $k_{\parallel}$ (in the repeated zone scheme) moves along $\bar{K}\bar{M}$ after passing $\bar{K}$. The most prominent feature of the spectra around $\bar{\Gamma}$ ($\theta = 0°$) is the broad and unresolved structure at the top of the valence band. On the way from $\bar{\Gamma}$ to $\bar{K}$ (at $\theta \approx 30°$–$35°$) two strong peaks dominate the spectra at emission angles larger than $\sim 10°$. One disperses ~ 1.5 eV down to $\bar{K}$ where it mixes with another peak and is reduced in intensity, while it gains in intensity again further along the $\bar{\Gamma}\bar{K}\bar{M}$ direction as it disperses upwards approaching $\bar{M}$ at $\theta \approx 50°$. The other peak disperses more weakly and decreases in intensity between $\bar{K}$ and $\bar{M}$. There is possibly a trace of emission from the conduction band in the $\theta = 48.5°$ spectrum close to

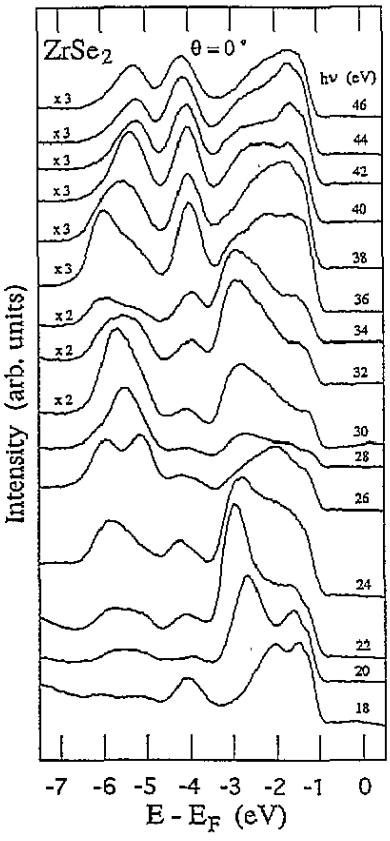

Figure 2. Normal emission EDCs for $ZrSe_2$ with $h\nu = 18$–46 eV.

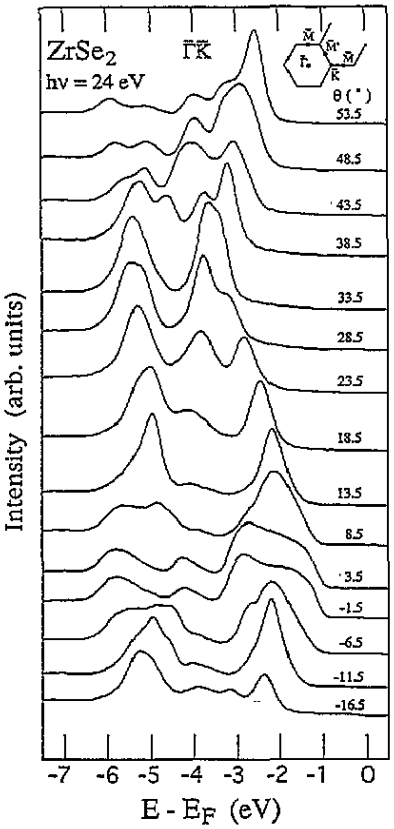

Figure 3. EDCs for $ZrSe_2$ in the $\bar{\Gamma}\bar{K}$ azimuthal direction with $h\nu = 24$ eV and polar angle $\theta = -16.5°$ to 53.5°.

$\bar{M}$, where the conduction band has its minimum. This very weak feature is only detectable if that part of the spectrum is enlarged (and thus is not observed in figure 3) and should therefore be considered as doubtful.

EDCs recorded with $h\nu = 24$ eV and 38 eV in the $\bar{\Gamma}\bar{M}$ azimuthal direction are shown in figure 4. The polar angle θ ranges from $-15°$ to 55°. The spectra for $h\nu = 24$ eV shows, in addition to a weakly dispersive band 4 eV below E_F, an upper part with bands dispersing downwards from $\bar{\Gamma}$ to a minima at $\bar{M}$ ($\theta \approx 25°$–$30°$), where it is reduced in intensity, and a lower part where the peak at the valence band bottom dominates at emission beyond $\bar{M}$. Around $\bar{M}$, emission from the conduction band is weakly visible for $\theta = 25°$ and 30°. The spectra for $h\nu = 38$ eV differ quite drastically in peak intensities, due to the different cross-sections for the photoemission process as the photon energy is changed. The higher photon energy also makes it possible to observe transitions from $\bar{\Gamma}$ ($\theta \approx 40°$–$45°$) of the next repeated Brillouin zone, and beyond. Emission from the conduction band is visible around $\bar{M}$ (at $\theta \approx 20°$ for this photon energy).

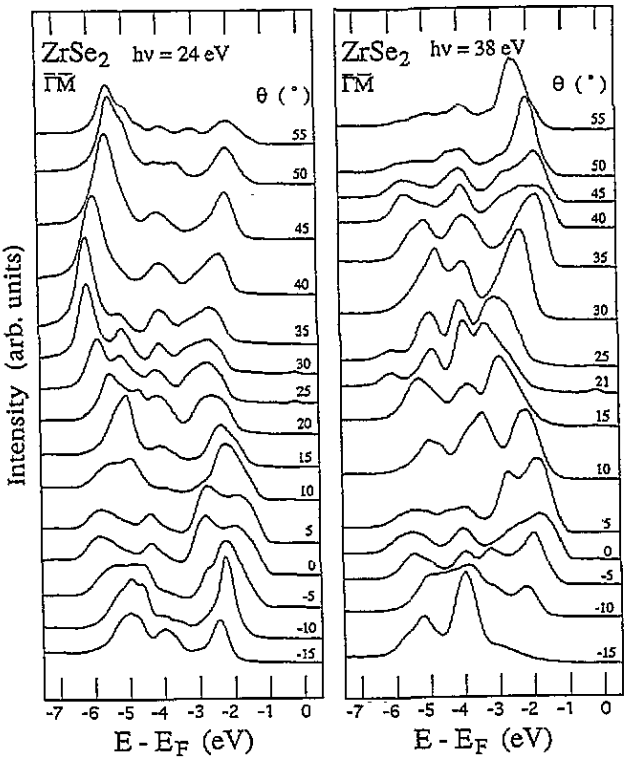

Figure 4. EDCs for $ZrSe_2$ in the $\bar{\Gamma}\bar{M}$ azimuthal direction with polar angle $\theta = -15°$ to 55°, $h\nu = 24$ eV (left panel) and $h\nu = 38$ eV (right panel).

4.2. Cs_xZrSe_2

The deposition of Cs onto the $ZrSe_2(0001)$ surface and the intercalation process were monitored by recording Cs 4d core level spectra with photon energy $h\nu = 100$ eV (obtained using second-order grating diffraction). The Cs 4d spectra in figure 5(*a*) clearly show the spin–orbit splitting of 2.2 eV between the $4d_{3/2}$ and $4d_{5/2}$ levels, and a further splitting indicating the presence of Cs in two different forms. From a comparison with the study by Pettenkofer *et al* [10], the sharp and more intense spin–orbit split pair (I_1, I_2) at lower binding energy is identified as intercalation induced, while the weaker and more broadened pair (S_1, S_2) at higher BE is identified as originating from Cs remaining at the surface. The surface peak S_2 is obscured by emission from the Zr 4p core level (excited by first-order radiation with $h\nu = 50$ eV). The BE of the intercalation peak I_1 is 76.3 eV, and for the surface peak S_1 it is 77.4 eV. The separation between I_1 and S_1 is then 1.1 eV. An additional Cs deposition, made seven hours after the initial one, induced only minor changes in the spectra, indicating that continued Cs deposition mainly increases the intercalation depth without changing the near-surface composition, and that once deposited, the Cs atoms are rapidly ionized and subsequently intercalated into the interior of the sample.

In order to study possible intercalation-induced effects on the core levels of the outermost chalcogenide atomic layers, Se 3d core level spectra were recorded with photon energy $h\nu = 130$ eV. The spectrum from pure $ZrSe_2$, curve A in the left panel of figure 5(*b*), shows the spin–orbit-split $3d_{3/2}$ and $3d_{5/2}$ levels, with the $3d_{5/2}$ level significantly higher in intensity. The BEs are: ($3d_{3/2}$) 55.2 eV and ($3d_{5/2}$) 54.5 eV. Immediately after the first Cs

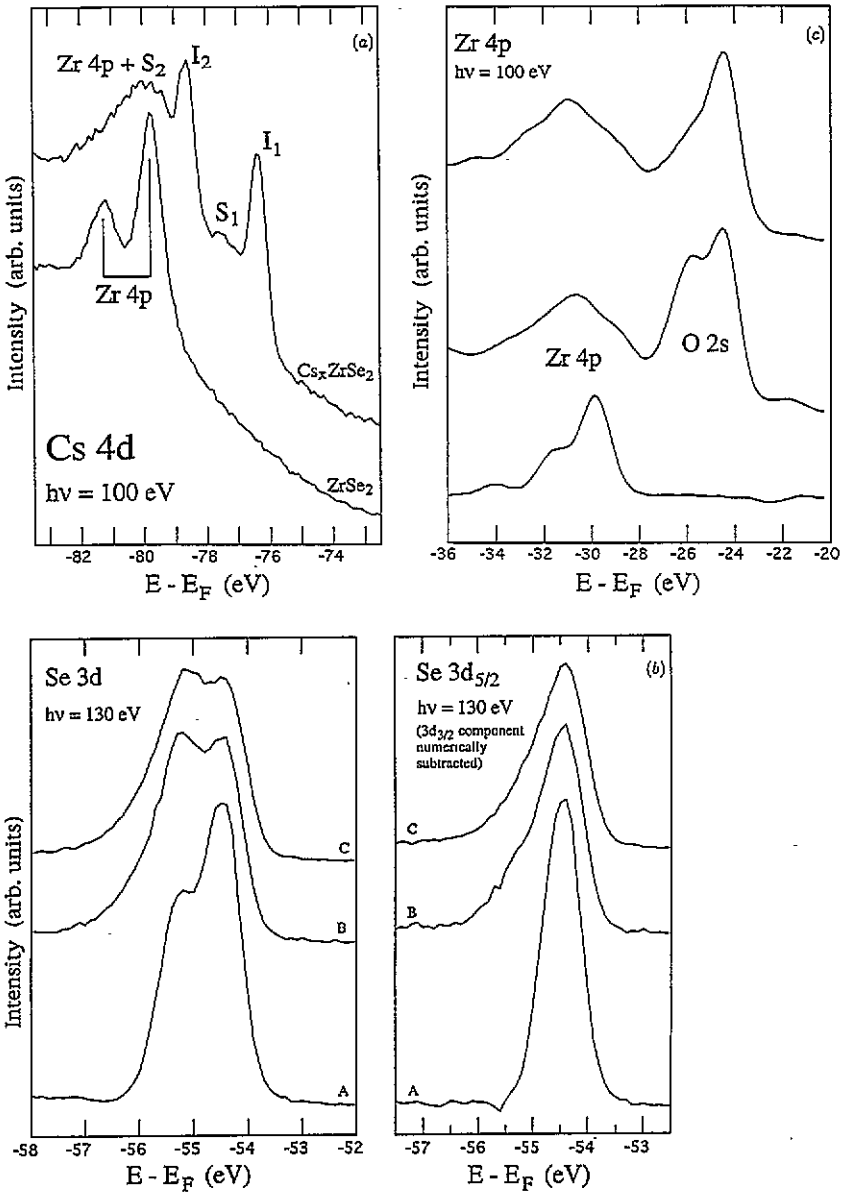

Figure 5. Core level spectra of (*a*) Cs 4d with $h\nu = 100$ eV, before and after the initial Cs deposition onto the (0001) surface of $ZrSe_2$. Two pairs of spin–orbit-split peaks are indicated, (I_1, I_2) and (S_1, S_2), corresponding to intercalated Cs and Cs remaining at the sample surface. The pair of Zr 4p peaks (excited with $h\nu = 50$ eV) obscures the surface peak S_2. (*b*) Left panel: Se 3d core level spectra with $h\nu = 130$ eV, before and after Cs depositions onto $ZrSe_2$. A: spectrum from $ZrSe_2$ before Cs deposition. B: immediately after one Cs deposition. C: after a second Cs deposition made seven hours after the initial one (recorded eight hours after the second deposition). Right panel: Se $3d_{5/2}$ core level after the $3d_{3/2}$ level has been numerically subtracted. A, B and C correspond to the same conditions as in the left panel. (*c*) Zr 4p core level spectra with $h\nu = 100$ eV, before and after Cs depositions. Lower curve: before Cs deposition. Middle curve: after the second Cs deposition made seven hours after the initial one (recorded one hour after the second deposition). Upper curve: after the second Cs deposition (recorded eight hours after the second deposition).

deposition, the spectrum has changed (curve B, left panel) in that the $3d_{3/2}$ level appears somewhat more intense than the $3d_{5/2}$ level. The BEs do not change, but the lineshapes are different. The high-BE side of the $3d_{3/2}$ level is far more asymmetric after Cs deposition; this asymmetry is possibly slightly increased after the second deposition (curve C, left panel, recorded eight hours after the second deposition), where the $3d_{5/2}$ intensity also apparently decreases somewhat further relative to the $3d_{3/2}$ level. The BE of the $3d_{3/2}$ level has now changed to 55.1 eV, while the $3d_{5/2}$ level remains at 54.5 eV. In the right panel of figure 5(*b*), the $3d_{3/2}$ component has been numerically subtracted so that the lineshape of the $3d_{5/2}$ level can be more closely studied. The increased asymmetry following intercalation is very evident (the curves A, B and C in the right panel correspond to A, B and C in the left).

In figure 5(*c*), the Zr 4p core level is shown, along with a growing O 2s feature due to increasing contamination of the surface. Due to the relatively low signal-to-noise ratio of the data, the spectra have been smoothed, which could introduce some slight distortions compared with the original data. The spectrum for pure $ZrSe_2$ (lower curve) shows the pair of Zr $4p_{1/2}$ and $4p_{3/2}$ levels recorded with $h\nu = 100$ eV. The peaks are weak in intensity, but no trace of contamination is visible in this energy range, where O 2s levels are assumed to appear. The middle curve shows the spectrum after two Cs depositions (recorded one hour after the second one). The Zr 4p peaks are now smeared out so that the spin–orbit splitting is not resolved, and the emission is also significantly broadened. The dominating features are now two peaks, which appear at BEs of 25.8 eV and 24.4 eV respectively, attributed to the O 2s levels. The upper spectrum is recorded after two Cs depositions but now eight hours after the second one. The main difference from the middle curve is that the O 2s level at BE 25.8 eV decreases in intensity and is only seen as a shoulder on the other peak. The emission from the Zr 4p level is quite the same in the middle and upper curves.

Normal emission EDCs as well as EDCs in the $\bar{\Gamma}\bar{K}$ and $\bar{\Gamma}\bar{M}$ azimuthal directions were recorded in the valence band region to study the possible changes induced by the Cs intercalation. The normal emission EDCs for Cs_xZrSe_2 reveal a valence band with non-dispersing features along the ΓA symmetry direction. In sharp contrast to pure $ZrSe_2$ (figure 2) the spectral peaks in figure 6 of the Cs-intercalated compound do not, within experimental resolution, disperse at all with photon energy, i.e. the Cs intercalation has decoupled adjacent layers and induced a transition of the valence band from 3D to 2D character. The peak at BE 2.7 eV dominates at all photon energies. The top of the valence band is best seen at the lower photon energies while the bottom is strongest between 22 and 36 eV. Emission from the conduction band can be seen over the entire photon energy range, although of very low intensity at $h\nu = 28$ eV. At $h\nu = 26$ and 38 eV there appears a weak structure just below the conduction band emission and not clearly resolved from it. This feature is probably emission from the intercalated Cs 4d core level, excited with higher-order grating diffraction (fourth and third order respectively). The primarily Se 4p-derived valence band appears to have a maximum intensity at $h\nu = 24$ eV, while the emission from the mainly Zr 4d-derived conduction band has a minimum in intensity at $h\nu = 28$ eV.

EDCs in the $\bar{\Gamma}\bar{K}$ azimuthal direction with $h\nu = 24$ eV are shown in figure 7 for $\theta = 0°$–$60°$. In contrast to pure $ZrSe_2$ (figure 3), emission from the conduction band can be seen at all angles, with a small maximum around $\bar{M}$ ($\theta \approx 45°$–$50°$). The differences in peak intensities between the pure and the Cs-intercalated substrate are striking, although the energy positions of the peaks appear to be less affected. Two peaks dominate at small emission angles, the upper dispersing upwards at first then downwards and mixing with another peak at $\bar{K}$ ($\theta \approx 30°$–$35°$) and then dispersing upwards again towards $\bar{M}$ ($\theta \approx 55°$);

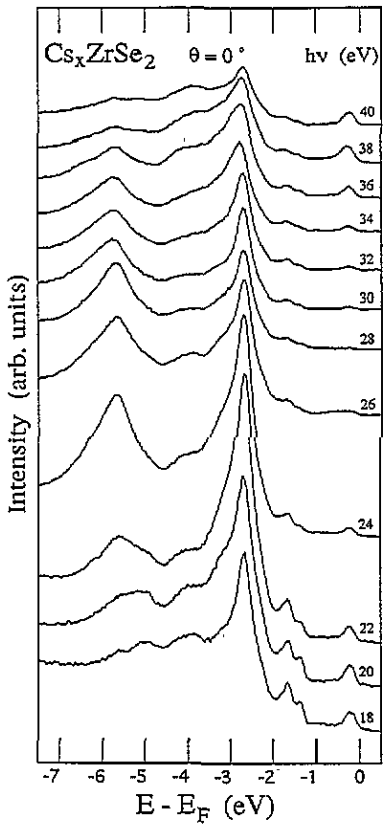

Figure 6. Normal emission EDCs for Cs-intercalated $ZrSe_2$ with $h\nu = 18$–40 eV.

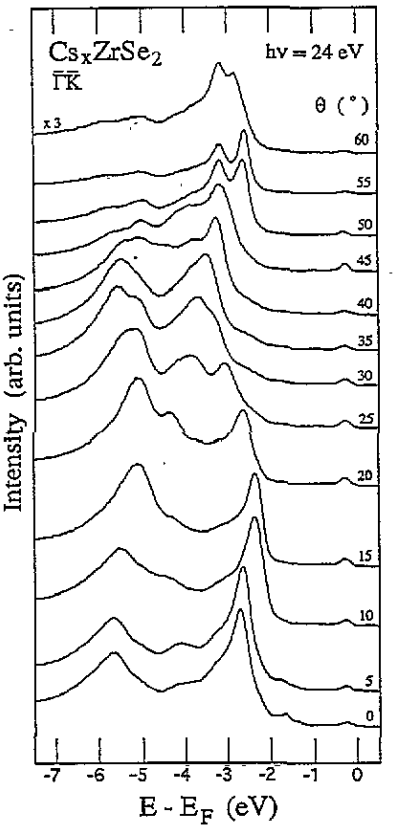

Figure 7. EDCs for Cs-intercalated $ZrSe_2$ in the $\bar{\Gamma}\bar{K}$ azimuthal direction with $h\nu = 24$ eV and $\theta = 0°$–60°.

the other, more broadened peak disperses less and mixes with another at $\bar{K}$, and decreases markedly in intensity towards $\bar{M}$.

Figure 8 shows EDCs recorded in the $\bar{\Gamma}\bar{M}$ azimuthal direction with $h\nu = 24$ eV for $\theta = 0°$–60°. The differences in peak intensities compared with pure $ZrSe_2$ (figure 4) are just as striking as for the $\bar{\Gamma}\bar{K}$ azimuthal direction, but similarly the peak positions appear to be less affected. The most striking effect of the intercalation is the greatly enhanced emission from the conduction band around $\bar{M}$ ($\theta \approx 25°$–30°). Emission from the conduction band is visible through the entire BZ as for the $\bar{\Gamma}\bar{K}$ direction, but the electron pocket around $\bar{M}$ is now so enlarged by charge transfer from the Cs that the peak shows experimental dispersion. The valence band emission is dominated for almost every angle by the strong, very dispersive peak in the upper part and the more broadened one in the bottom part.

5. Discussion

5.1. $ZrSe_2$

The normal emission spectra in figure 2 of the pure compound, with spectral features that disperse with varying photon energy, make it clear that the valence bands of $ZrSe_2$ are of 3D character. This picture is supported by the LAPW band calculation presented in

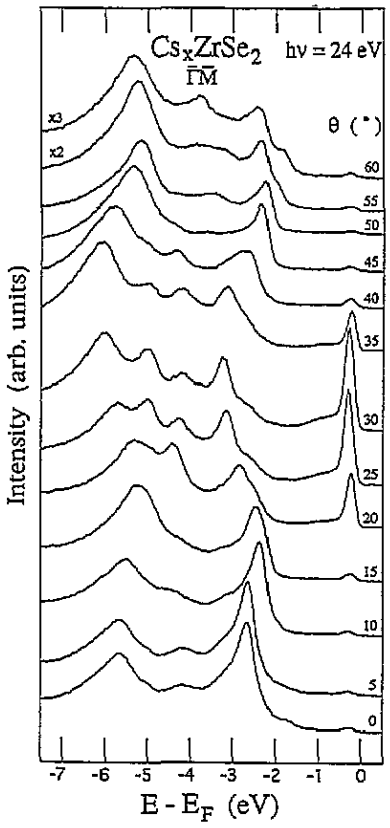

Figure 8. EDCs for Cs-intercalated $ZrSe_2$ in the $\bar{\Gamma}\bar{M}$ azimuthal direction with $h\nu = 24$ eV and $\theta = 0°$–$60°$.

figure 1(a), where one of the upper valence bands disperses by more than 2 eV downwards from Γ to A, and another at the bottom of the valence band disperses by more than 1 eV upwards from Γ to A. The experimental dispersions of the structures are not as large as in the calculations. In the spectra there is an almost dispersionless band at a BE of 4 eV which is consistent with a very flat and doubly degenerate band in the calculations. The absence of dispersion of the feature at the top of the valence band implies a flat top to the valence band along the ΓA direction, and is also in agreement with the calculation, where there is a doubly degenerate band with only 0.2 eV dispersion between Γ and A.

The valence bands of $ZrSe_2$ show, as expected, strong dispersion parallel to the layers. The excess of zirconium gives $ZrSe_2$ extrinsic properties, and the extra electrons occupy the lowest levels in the conduction band, located as small electron pockets centred on the BZ boundaries along the LML lines. Klipstein *et al* [28] have investigated $ZrSe_2$ crystals and found electron concentrations of $\sim 5 \times 10^{19}$ cm^{-3}. We assume that this value should be valid for the $ZrSe_2$ crystal examined here since it is likely that it comes from the same growth batch, or at least has been grown under very similar conditions. (Onuki *et al* [29] have determined the electron concentration at room temperature to be 3.8×10^{19} cm^{-3} for $ZrSe_2$ single crystals grown with good stoichiometry.) The electron pocket can be seen in the spectra of figure 4, but the emission from it is weak and only detectable over a limited range of angles. It must be small since there is possibly just a trace of it (clearly not resolvable in figure 3, but in our original data) in the $\bar{\Gamma}\bar{K}$ direction where the $\theta = 48.5°$ spectrum is close to the $\bar{M}$ point. (One reaches $\bar{M}$ with $\theta = 47.8°$ for this photon energy.) The dimensions of this electron pocket can be estimated in a similar fashion as has been

done by Traum *et al* for $TiSe_2$ [30] and Barry *et al* for TiS_2 [31]. Assuming that the electron pocket has an elliptical shape, we obtain the semi-major axis to be ≈0.18 ΓM (0.17 $Å^{-1}$). The semi-minor axis is approximated as ≈0.02 KM (0.01 $Å^{-1}$), but as there is no clear conduction band emission in this direction, this value is rather approximate. The half-axis dimension in the c direction is assumed to be ≈0.5 LM (≈0.25 $Å^{-1}$), an approximation also used by Traum *et al* [30] and Barry *et al* [31]. From these values, we estimate the electron pockets to occupy ≈0.12% of the BZ. This would then correspond to a carrier concentration of 1.1×10^{19} cm^{-3}, in rather good agreement with Klipstein *et al* [28] (and also with Onuki *et al* [29]) when one considers the uncertainties in estimating the electron pocket size. From the carrier concentration the amount of excess Zr is estimated; we find x in $Zr_{1+x}Se_2$ to be about 0.0006.

Following Hughes and Liang [32], the measured EDCs were reduced to experimental structure plots where the initial energy is plotted as a function of $k_\parallel$, the wavevector component parallel to the surface. For each peak $k_\parallel$ is given (in $Å^{-1}$) by the relation $k_\parallel = 0.512\sqrt{E_k}\sin\theta$, where E_k is the kinetic energy of the photoelectron in eV.

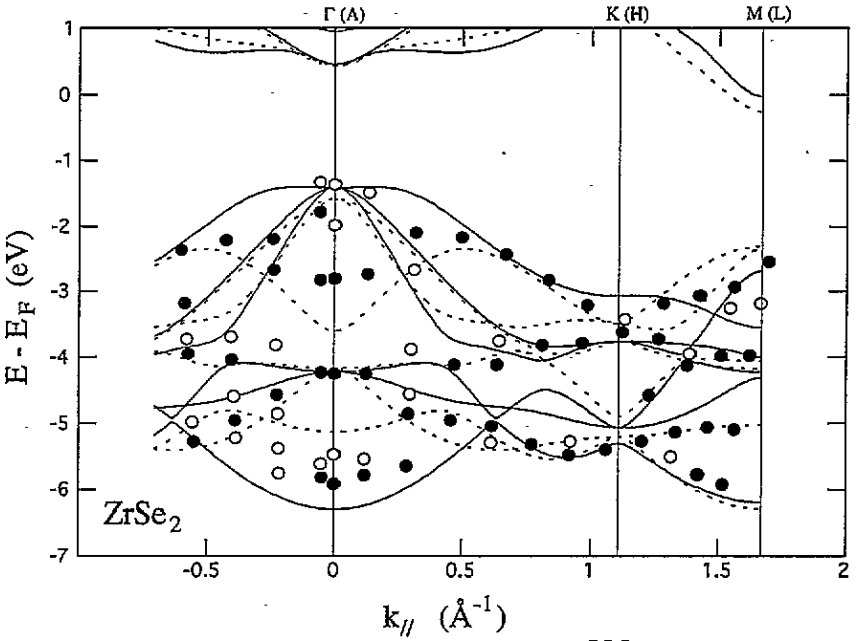

Figure 9. Structure plot for $ZrSe_2$ along the $\bar{\Gamma}\bar{K}\bar{M}$ direction. Filled circles correspond to conspicuous spectral peaks in figure 3, open circles to weaker structures. Comparisons are made with ΓKM (full lines) and AHL (dashed lines) bands calculated by the LAPW method, and adjusted as described in the main text.

The experimental structure plots are presented and compared with the calculated LAPW bands along ΓKM and AHL in figure 9 and the bands along ΓM and AL in figure 10. The calculated conduction bands have been shifted upwards by 1.0 eV relative to the valence bands to obtain best agreement with the experimental data. As $k_\perp$, the wavevector component perpendicular to the surface, is experimentally undetermined, experimental points appearing in between associated bands are also consistent with the calculations. When this is considered, the agreement between experimental and calculated bands is generally

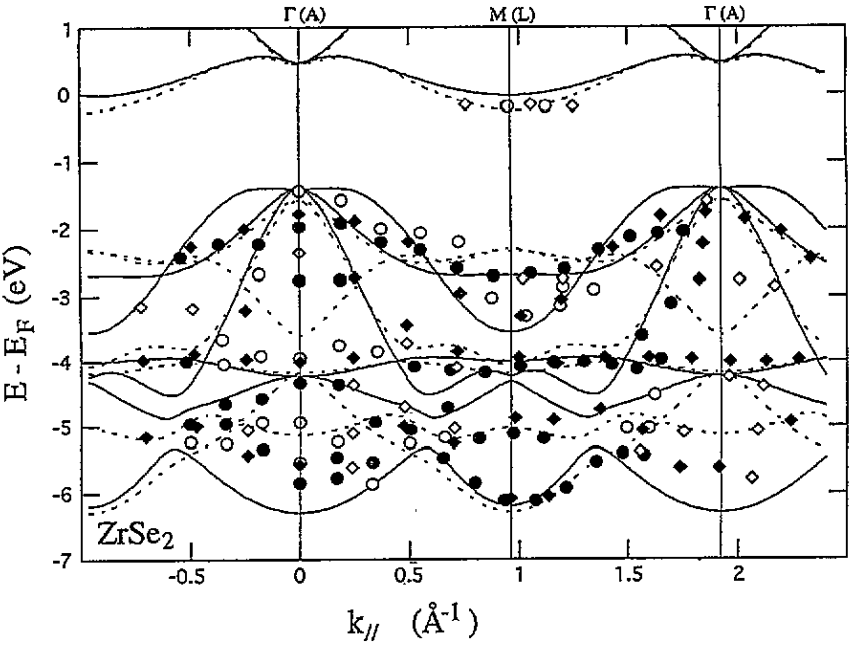

Figure 10. Structure plot for $ZrSe_2$ along the $\bar{\Gamma}\bar{M}$ direction. Filled circles (diamonds) correspond to conspicuous spectral peaks in figure 4 with $h\nu = 24$ eV (38 eV), open circles (diamonds) to weaker structures. Comparisons are made with ΓM (full lines) and AL (dashed lines) LAPW bands adjusted as described in the main text.

very good for both azimuthal directions, and most spectral features can be identified in terms of the calculated bands.

Table 1. Band structure characteristics for $ZrSe_2$ and Cs_xZrSe_2. Comparison is made with other calculations and experimental data for $ZrSe_2$. All entries are in eV.

		$ZrSe_2$					
	Present	(i)	(ii)	(iii)	(iv)	(v)	Cs_xZrSe_2
E_g	1.1	1.0	1.4	1.3; 0.75	1.2		1.0
VBW (experimental)	4.8					5.8	4.7
VBW (calculated)	4.9	5.4	3.3	4.9; 4.7			4.8

(i) Pseudopotential, [1].
(ii) Semi-empirical tight binding/LCAO, [19].
(iii) Self-consistent symmetrized OPW, [20], [21].
(iv) Optical absorption edge measurement, [33].
(v) XPS measurement, [23].

Since the electron pocket at $\bar{M}$ is detectable, we are able to determine experimentally the p–d band gap of $ZrSe_2$, finding a value of 1.1 eV. The valence band maximum (VBM) is at the zone centre and the conduction band mimumum (CBM) at $\bar{M}$ so the band gap is indirect. (The calculation actually locates the CBM at L.) This value could however be slightly underestimated as the VBM is seen as a shoulder at best, and the weak emission from the conduction band might be from the tail of the CBM peak reaching just below E_F. We also find the valence band width (VBW) to be 4.8 eV, which agrees well with the

calculated band width of 4.9 eV. These values are compared with other experimental and calculated values in table 1. The value of the band gap reported by Lee *et al* [33] is close to our value, but the band width reported by Jellinek *et al* [23] is somewhat large. The semiempirical tight-binding calculation by Bromley and co-workers [19] is not consistent with our results, but the chemical pseudopotential calculation by Bullett [1] and the self-consistent symmetrized OPW calculations by Isomäki *et al* [20, 21] agree quite well with our experimental data and our calculated bands.

5.2. Cs_xZrSe_2

The intercalation process is often described and interpreted within the rigid-band model, which assumes that the host valence band structure remains unchanged upon intercalation, except that the band filling is altered due to charge transfer from the intercalant to the host lattice.

After intercalation with Cs, the normal emission spectra of Cs_xZrSe_2 in figure 6 show a valence band where the structures do not disperse at all within the experimental resolution. The Cs intercalation has thus induced a transition from 3D to 2D character of the valence band, in conflict with the rigid-band model, in that adjacent layers have been decoupled by the intercalated Cs ions. To what extent is this 2D character reflected in the calculation? The two dispersive bands from pure $ZrSe_2$ still show dispersion along ΓA (figure 1(*b*)), but significantly less than before (0.8 and 0.6 eV compared to 2.2 and 1.2 eV respectively). This is not consistent with the measurements, where the corresponding peaks do not show any dispersion of this magnitude. Similar reductions of band dispersions perpendicular to the layers have been suggested by band calculations for $LiTiS_2$ [34–36] and for $NaTiS_2$ [36], although for these lighter alkali metals the interlayer separation is not increased to the same extent as that for Cs.

The experimental structure plots for Cs_xZrSe_2 along the $\bar{\Gamma}\bar{K}$ and $\bar{\Gamma}\bar{M}$ azimuthal directions are presented and compared with corresponding LAPW bands along ΓKM and AHL in figure 11 and along ΓM and AL in figure 12. The calculated conduction bands have now been shifted upwards by 0.75 eV relative to the valence bands. The agreement between experimental and calculated bands is very good overall, the main exception being the conduction band where the calculated bands are about 0.5 eV above the Fermi level for most of the BZ, while weak emission is still seen. This weak emission close to E_F over much of the BZ therefore probably originates from indirect transitions and scattering, and stronger emission occurs at M (L) itself where the CBM is located. Most of the spectral features can be readily identified in terms of calculated bands.

The changes in the structure of the valence and conduction bands of Cs-intercalated $ZrSe_2$ provide evidence that the rigid-band model is not applicable to this intercalation compound. The calculated CBM, located at the L point along the AL direction for $ZrSe_2$, is located at the M point after intercalation, since the lowest-lying ΓM conduction band is pulled down 0.4 eV below the corresponding AL band around M and all the way between K and M. This conduction band feature shows considerable differences regarding peak intensity for the $\bar{\Gamma}\bar{K}\bar{M}$ and $\bar{\Gamma}\bar{M}\bar{\Gamma}$ directions in figures 7 and 8. In the $\bar{\Gamma}\bar{K}\bar{M}$ direction the CBM is reached for $h\nu = 24$ eV at $\theta = 48.4°$, but the spectra at 45° and 50° show only a modest increase in the intensity for this peak, which suggests a limited extent of the electron pocket in the $\bar{K}\bar{M}\bar{K}$ direction. In the $\bar{\Gamma}\bar{M}$ direction, however, this peak is greatly enhanced over a range of angles of at least 20° to 35°, indicating a much larger extent in this direction.

The dimensions of the electron pocket are estimated as for $ZrSe_2$, but now we assume

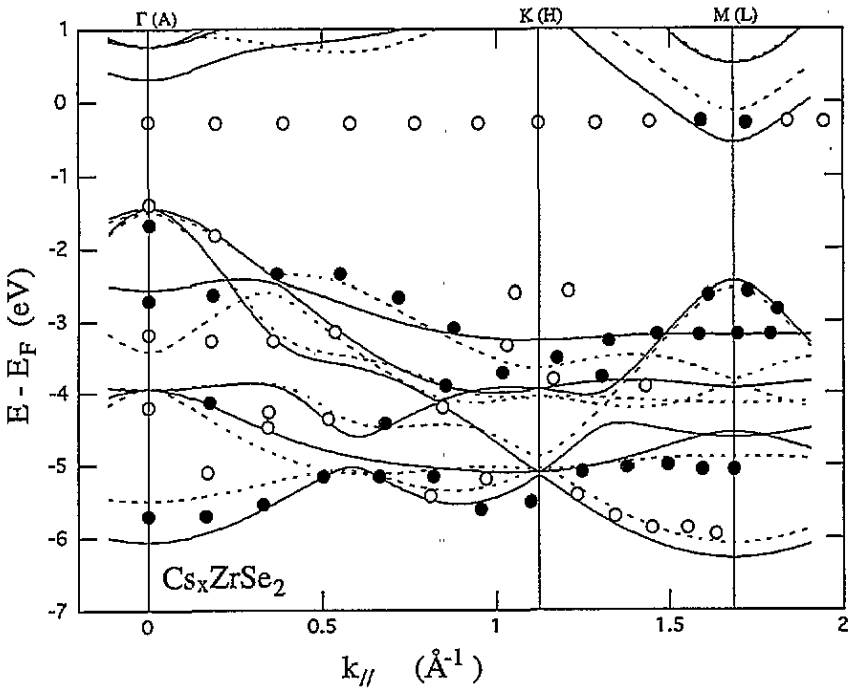

Figure 11. Structure plot for Cs-intercalated $ZrSe_2$ along the $\bar{\Gamma}\bar{K}\bar{M}$ direction. Filled circles correspond to conspicuous spectral peaks in figure 7, open circles to weaker structures. Comparisons are made with ΓKM (full lines) and AHL (dashed lines) LAPW bands adjusted as described in the main text.

that the electron pocket extends through the whole BZ between LML, thus extending 0.72 $Å^{-1}$ in the c direction. The semi-major axis is ≈0.4 ΓM (0.35 $Å^{-1}$) and the semi-minor axis is ≈0.15 KM (0.08 $Å^{-1}$). From these values we estimate the electron pockets to occupy 8.1% of the BZ, which corresponds to a carrier concentration of 5.1×10^{20} cm^{-3}. The Cs concentration can now be estimated by assuming that every intercalated Cs atom donates one electron, and we find the Cs concentration $x \approx 0.16$. The carrier concentration is larger than that found for pure $ZrSe_2$ by a factor of 50, and can be compared to $LiZrSe_2$, where carrier concentrations of 7×10^{21} cm^{-3} and 1.2×10^{22} cm^{-3} for bulk intercalated samples were reported [28, 37]. This difference can be partly explained by the lower alkali concentration (0.16 compared to 1) and by the larger unit cell due to the expansion along the c axis for Cs_xZrSe_2, but also by errors introduced by the finite angular acceptance of the energy analyser (±2°). Considering the arbitrariness of the estimated electron pocket size, the estimated value of the carrier concentration found for Cs_xZrSe_2 is in rather good agreement with the $LiZrSe_2$ values; the estimated Cs concentration also appears reliable.

The peak intensities vary drastically in the valence band region between the pure and the Cs-intercalated material, and the calculated ΓKM (AHL) and ΓM (AL) bands reflect the 3D to 2D transition by a large reduction of the perpendicular dispersion. But the calculated dispersion is still not zero; at most parts of the BZ this dispersion is only some tenths of an eV, but at the zone centre there are larger differences, as discussed earlier, and at M and L there are bands with 0.6 eV and 0.4 eV perpendicular dispersions respectively. At the CBM the perpendicular dispersion is 0.4 eV. The experimental bands agree very well with the calculated bands, though two features are observed which are not apparent in the

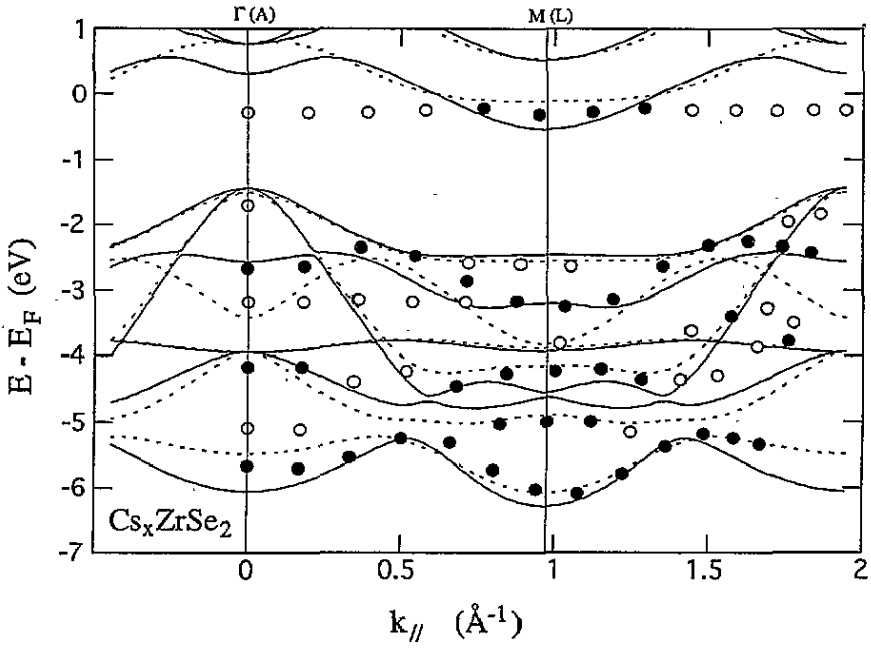

Figure 12. Structure plot for Cs-intercalated $ZrSe_2$ along the $\bar{\Gamma}\bar{M}$ direction. Filled circles correspond to conspicuous spectral peaks in figure 8, open circles to weaker structures. Comparisons are made with ΓM (full lines) and AL (dashed lines) LAPW bands adjusted as described in the main text.

calculations, a weak feature at the zone centre, visible in both the $\bar{\Gamma}\bar{K}$ and $\bar{\Gamma}\bar{M}$ directions, some 5.1 eV below E_F, and another one around $\bar{K}$ at 2.6 eV below E_F; this possibly extends further away from $\bar{K}$ since the emission for the 25° and 40° spectra is clearly asymmetric, but no spectral peak can be resolved. These two features are probably due to indirect transitions from critical points with high 2D density of states (DOS).

The indirect p–d band gap of Cs_xZrSe_2 was experimentally determined to be 1.0 eV, a slight decrease compared to pure $ZrSe_2$ (table 1). Both the VBM and the CBM peaks are now well defined, so the determination of the band gap of Cs_xZrSe_2 is more accurate than for pure $ZrSe_2$. The experimental valence band width was determined to be 4.7 eV (slightly less than for $ZrSe_2$), in excellent agreement with the calculated band width of 4.8 eV (table 1). The intercalation-induced effects on the band gap and the valence band width are rather small: the band gap decreases slightly and so does the valence band width. Comparing this with the isoelectronic TiS_2, for which the band gap increases 0.7 eV and the valence band width decreases 0.8 eV upon Cs intercalation [15], there is a large difference; this might be due to electrostatic effects i.e. the coulombic repulsion between interlayer chalcogen atoms, which is decreased as the Cs ions enter the intersandwich gaps. These effects are supposedly much larger for TiS_2 than for the less ionic $ZrSe_2$.

We do not have a ready explanation of the discrepancy between experiments and calculations regarding the 3D to 2D transition of the valence band structure. There is one rather trivial possibility that the structural parameters of the intercalation compound differ from the ones used in the calculations, but the impressive agreement found in figures 11 and 12 suggests that the parameters used are quite accurate. It has been reported that the 1T structures might undergo structural rearrangements when intercalated with alkali metals.

The coordination of the alkali metal in the van der Waals gaps can be either octahedral or trigonal prismatic depending on the alkali metal concentration and size, and also on the covalency of the host structure [38, 39]. In general, trigonal prismatic coordination is expected for the heavier alkali metals. The structure in each sandwich remains intact, but adjacent sandwiches must be displaced to produce a trigonal prismatic coordination of the alkali ion; thus the layer stacking is changed to a 3R structure, where the conventional unit cell consists of three TX_2 sandwiches with intercalated alkali atoms in between. Although the conventional unit cell of the 3R structure is three times larger in the c direction, the primitive unit cell, which is now rhombohedral, contains the same number of atoms as the unit cell in the assumed 1T structure of $CsZrSe_2$. The arguments above suggest that the intercalated Cs atoms have trigonal prismatic coordination contrary to what is assumed in our calculations. Since this structural transformation occurs for 'bulk-intercalated' samples one might argue whether samples intercalated by deposition in UHV really undergo this structural change or whether they stay in a metastable intercalated 1T structure. Other possibilities which could explain the absence of perpendicular dispersion are that the intercalation has induced substantial layer–layer stacking disorder, or that the interlayer coupling may in fact be further weakened by many-body effects not included in the calculations. These matters needs to be studied further before a satisfactory explanation can be put forward.

Table 2. Cs core level BE when deposited onto different TMDCs. The BE of the intercalation-induced and surface Cs $4d_{5/2}$ (or $5p_{3/2}$) peaks I_1 and S_1 are given along with the separation ΔBE between the metallic bulk $4d_{5/2}$ ($5p_{3/2}$) component and I_1. The BEs of the metallic bulk core levels are: 77.3 eV ($4d_{5/2}$) and 11.8 eV ($5p_{3/2}$) [40, 41]. (Cs is reported to be adsorbed on WSe_2 [11] and MoS_2 [42], without intercalation taking place.)

	I_1 (eV)	S_1 (eV)	ΔBE (eV)
Cs/TiS_2[a]	75.8	76.8	1.5
$Cs/ZrSe_2$[b]	76.3	77.4	1.0
Cs/VSe_2[a]	75.8	77.0	1.5
$Cs/2H\text{-}TaSe_2$[c]	10.5 (5p)	11.8 (5p)	1.3

[a] [15].
[b] This paper.
[c] [10].

The BEs of the Cs $4d_{5/2}$ and $4d_{3/2}$ levels I_1 and I_2 in figure 5(a) are 76.3 and 78.5 eV respectively for the intercalated species; for the surface species the corresponding peak S_1 has a BE of 77.4 eV, while S_2 should appear at 79.6 eV but is obscured by emission from the broadened Zr 4p core level. There are only a few photoemission investigations reported for other Cs-intercalated TMDC systems [3, 10, 11, 15], and the BEs of the core levels of the intercalated and surface Cs are summarized in table 2. One important contribution to the difference in BEs for peak I_1 might be the different shifts of the Fermi level as electrons are transferred to the host layers. These shifts will depend on the widths of the lowest conduction band in both pure and intercalated crystals, and on the total charge transferred. It is not possible to determine the Cs concentration from the Cs 4d spectral intensities due to normalization problems associated with the use of second-order grating diffraction radiation. Therefore we do not have any other method to compare the estimated Cs concentration $x \approx 0.16$ as obtained from the electron pocket size.

The main changes in the Se 3d core level spectra shown in figure 5(b) upon intercalation are the apparent decrease in the relative intensity of the Se $3d_{5/2}$ level, and the increased asymmetry—the development of a tail to higher BE. The apparent intensity behaviour may

be due to the increased asymmetry of the lineshapes, in that the $3d_{3/2}$ level is based on a higher background. This intensity variation is rather similar to that reported for Li/WSe_2 [12], Li/$TiSe_2$ [13] and Cs/$TaSe_2$ [10], although more pronounced in this case. The BE of the $3d_{5/2}$ level remains 54.5 eV throughout the measurements, while there is a small change (within experimental error limits) for the $3d_{3/2}$ level from 55.2 to 55.1 eV in the last spectrum; this could well be due to the increased asymmetry, so the intercalation does not apparently induce any shift of the Se 3d levels. The data in the right panel show that the full width at half maximum (FWHM) of the $3d_{5/2}$ level increases markedly. For pure $ZrSe_2$ the FWHM is 0.8 eV, while the FWHM of the $3d_{5/2}$ level for Cs_xZrSe_2 has increased 25% to 1.0 eV. A more thorough analysis of the core levels presented here and of similar alkali metal/TMDC systems is in preparation and will appear elsewhere [43].

The asymmetric lineshape of the Se 3d core level is probably due to a different screening of the core level hole created in the photoemission process. The conduction electrons tend to screen the core hole which gives rise to a range of many-electron excitations within the conduction band [44]. The energy for these excitations is supplied by the kinetic energy of the emitted photoelectron. Nozieres and De Dominics [45] have established the core level lineshapes of metals with the conduction electrons as s states in a free-electron gas, where the δ-function lineshape is modified by the screening response of the conduction electrons. Doniach and Sunjic [46] showed that this result appears as an asymmetric lineshape in the photoemission spectrum (the core level lines will have a characteristic tail on the high-BE side) when the finite lifetime of the core hole is accounted for. Since the screening depends on low-energy electron–hole excitations within the conduction band, it is strongly dependent upon the density of states close to the Fermi level [47]; the core level lineshapes of $ZrSe_2$ are thus likely to be affected by the increased occupation of the lowest conduction band upon intercalation. The symmetric lineshape of pure $ZrSe_2$ verifies the low density of low-energy electron–hole excitations within the conduction band, which is to be expected when, as concluded from the experimental data, the conduction band electron pockets have a very limited extent in k space. For the intercalated crystal however, the higher density of electrons in the lowest conduction band, verified by the strong emission from the much enlarged pocket around the $\bar{M}$ point, produces a stronger screening response, resulting in an asymmetry in the Se 3d lineshape. This lineshape supports the picture that Cs-intercalated $ZrSe_2$ is of a more metallic character than the extrinsic semiconductor $ZrSe_2$. A similar trend can be seen in the core level lineshape study by Scarfe and Hughes [48], where the Ta 4f lineshapes are studied for TaS_2 and the intercalated compounds $Mn_{1/4}TaS_2$ and $Co_{1/3}TaS_2$. The conduction bands in these materials are based principally on the cation d orbitals, so the screening carriers lie mostly in the planes of Ta and Zr atoms at the middle of the layer sandwich; the intercalation-induced asymmetry of the Se 3d core level here implies that the screening of the local electrostatic potential of the Se 3d holes, though remote from the mobile carriers, is nevertheless effective.

The changes of the Zr 4p core level already seen in figure 5(a) are confirmed by the spectra in figure 5(c). The spectrum for pure $ZrSe_2$ shows the spin–orbit-split 4p peaks, rather weak but clearly observable. The FWHM of the Zr $4p_{3/2}$ level is estimated to be 1.3 eV. After intercalation the emission has changed to a broad and still weaker structure that extends some 4 eV centred at 30.7 eV, probably with different smeared-out structures contributing. (The intercalated Cs 4d level can interfere, as the $4d_{5/2}$ and $4d_{3/2}$ levels can be excited by third-order grating diffraction ($h\nu = 150$ eV), and contribute to the spectra around BE 26.3 eV and 28.5 eV respectively.) This does not change in the last spectrum, eight hours after the second Cs deposition, where the emission is possibly weaker still. The FWHM is now estimated to be ~2.5 eV. Following the above discussion of the screening

effects of the intercalation-induced carriers, it would be expected that the Zr core lines would also become asymmetric; the broad features observed, and the relatively poor signal-to-noise ratio of the data, do not allow a firm observation of this effect, but it may well be contributing to the overall broadening of the Zr peaks.

The remaining features are from contamination of the surface by oxygen or CO. Now the BE of the O 2s level varies strongly for different systems (between 14 and 33 eV) [49]; this, combined with the fact that available studies of oxidized alkali metal concern the O 1s core level and/or the O 2p valence levels [50–52], but not the O 2s level, make any definite identification of the observed peaks difficult. The intercalated Cs 4d level should not interfere (but the $4d_{5/2}$ peak is possibly seen as a shoulder) with the two peaks which appear after the second Cs deposition, made seven hours after the initial one, with BEs of 24.4 and 25.8 eV (middle curve); this changes to a single peak at 24.4 eV with a shoulder at 25.8 eV in the topmost curve, obtained 15 h after the initial one and after no further Cs deposition. We believe that the peak at 24.4 eV, which increases in intensity between the second and the third spectra, is O 2s emission from caesium oxides, i.e. oxygen has reacted with Cs remaining at the surface. The feature at 25.8 eV is possibly from CO or O_2 adsorbed at the surface, which can desorb from the surface or dissociate to form caesium oxides with time, which could explain the reduction in intensity between the second and the third spectra.

6. Conclusions

$ZrSe_2$ is a layered extrinsic semiconductor, and it has been demonstrated, using photoelectron spectroscopy, that its electronic structure had 3D character. LAPW band calculations, which are in very good agreement with experimental bands, support this picture. After intercalation with Cs, the experimental data reveal that the valence band undergoes a transition from 3D to 2D character. The observed changes go far beyond the rigid-band model. This transition can be explained in terms of charge transfer to the host lattice and intercalation-induced decoupling of the substrate layers. The LAPW band calculations do not support this fully, as dispersion in the ΓA direction is still produced, but the agreement in the directions parallel to the layers is impressive. This discrepancy may have several explanations: the intercalated crystal may undergo structural rearrangements, possibly the intercalation has induced stacking disorder, or many-body effects further weaken the interlayer coupling. The band gap for pure and Cs-intercalated $ZrSe_2$ was determined with $E_g(ZrSe_2) = 1.1$ eV and $E_g(Cs_xZrSe_2) = 1.0$ eV; the experimentally determined valence band widths were 4.8 and 4.7 eV respectively, in excellent agreement with the calculated band widths 4.9 and 4.8 eV. The carrier densities of $ZrSe_2$ and Cs_xZrSe_2 are estimated to be 1.1×10^{19} cm^{-3} and 5.1×10^{20} cm^{-3} respectively, and the amount of excess Zr and Cs concentrations is estimated to be 0.0006 and 0.16 respectively. The asymmetric lineshape of the Se 3d core level after intercalation is explained by the higher density of electrons in the lowest conduction band, which gives rise to a different screening response of the created core level photohole.

Acknowledgments

This work was supported by the Swedish Natural Science Research Council. We also want to thank the staff at MAX-lab for their skillful assistance.

References

[1] Bullett D W 1978 *J. Phys. C: Solid State Phys.* **11** 4501
[2] Anderson O, Manzke R and Skibowski M 1985 *Phys. Rev. Lett.* **55** 2188
[3] Starnberg H I, Brauer H E, Holleboom L J and Hughes H P 1993 *Phys. Rev. Lett.* **70** 3111
[4] Friend R H and Yoffe A D 1987 *Adv. Phys.* **36** 1
[5] Liang W Y 1986 *Intercalation in Layered Materials* ed M S Dresselhaus (New York: Plenum) p 31
[6] Ashcroft N W and Mermin N D 1976 *Solid State Physics* (New York: Holt, Rinehart and Winston) p 385
[7] Whittingham M S 1978 *Prog. Solid State Chem.* **12** 41
[8] Rouxel J 1979 *Intercalated Layered Materials, Physics and Chemistry of Materials with Layered Structures* vol 6, ed F A Lévy (Dordrecht: Reidel) p 201
[9] Ohuchi F S, Jaegermann W, Pettenkofer C and Parkinson B A 1989 *Langmuir* **5** 439
[10] Pettenkofer C, Jaegermann W, Schellenberger A, Holub-Krappe E, Papageorgopoulos C A, Kamaratos M and Papageorgopoulos A 1992 *Solid State Commun.* **84** 921
[11] Papageorgopoulos C A, Kamaratos M, Papageorgopoulos A, Schellenberger A, Holub-Krappe E, Pettenkofer C and Jaegermann W 1992 *Surf. Sci.* **275** 314
[12] Schellenberger A, Jaegermann W, Pettenkofer C, Papageorgopoulos C A and Kamaratos M 1992 *Ber. Bunsenges. Phys. Chem.* **96** 1755
[13] Jaegermann W, Pettenkofer C, Schellenberger A, Papageorgopoulos C A, Kamaratos M, Vlachos D and Tomm Y 1994 *Chem. Phys. Lett.* **221** 441
[14] Schellenberger A, Jaegermann W, Pettenkofer C, Kamaratos M and Papageorgopoulos C A 1994 *Ber. Bunsenges. Phys. Chem.* **98** 833
[15] Brauer H E, Starnberg H I, Holleboom L J and Hughes H P 1995 *Surf. Sci.* **331–333** 419
[16] Pettenkofer C and Jaegermann W 1994 *Phys. Rev.* B **50** 8816
[17] Starnberg H I, Brauer H E, Nilsson P O, Holleboom L J and Hughes H P 1994 *Mol. Cryst. Liq. Cryst.* **244** 391
[18] Starnberg H I, Brauer H E, Holleboom L J and Hughes H P 1994 *Mod. Phys. Lett.* B **8** 1261
[19] Murray R B, Bromley R A and Yoffe A D 1972 *J. Phys. C: Solid State Phys.* **5** 746
[20] Isomäki H, von Boehm J and Krusius P 1979 *J. Phys. C: Solid State Phys.* **12** 3239
[21] Isomäki H and von Boehm J 1982 *Phys. Lett.* **89A** 89
[22] Shepherd F R and Williams P M 1974 *J. Phys. C: Solid State Phys.* **7** 4416
[23] Jellinek F, Pollak R A and Shafer M W 1974 *Mater. Res. Bull.* **9** 845
[24] Law A R, Andrews P T and Hughes H P 1991 *J. Phys.: Condens. Matter* **3** 813
[25] Vosko S H, Wilk L and Nusair M 1980 *Can. J. Phys.* **58** 1200
[26] Ceperley D M and Alder B J 1980 *Phys. Rev. Lett.* **45** 566
[27] Wilson J A and Yoffe A D 1969 *Adv. Phys.* **18** 193
[28] Klipstein P C, Pereira C M and Friend R H 1984 *Physics and Chemistry of Electrons and Ions in Condensed Matter (NATO ASI 130)* ed J V Acrivos, N F Mott and A D Yoffe (Dordrecht: Reidel)
[29] Onuki Y, Inada R and Tanuma S 1982 *J. Phys. Soc. Japan* **51** 1223
[30] Traum M M, Margaritondo G, Smith N V, Rowe J E and Di Salvo F J 1978 *Phys. Rev.* B **17** 1836
[31] Barry J J, Hughes H P, Klipstein P C and Friend R H 1983 *J. Phys. C: Solid State Phys.* **16** 393
[32] Hughes H P and Liang W Y 1973 *J. Phys. C: Solid State Phys.* **6** 1684
[33] Lee P A, Said G, Davies R and Lim T H 1969 *J. Phys. Chem. Solids* **30** 2719
[34] McCanny J V 1979 *J. Phys. C: Solid State Phys.* **12** 3263
[35] Umrigar C, Ellis D E, Wang D, Krakauer H and Posternak M 1982 *Phys. Rev.* B **26** 4935
[36] Dijkstra J, van Bruggen C F and Haas C 1989 *J. Phys.: Condens. Matter* **1** 4297
[37] Beal A R and Nulsen S 1981 *Philos. Mag.* B **43** 965
[38] le Blanc A, Danot M, Trichet L and Rouxel J 1974 *Mater. Res. Bull.* **9** 191
[39] Rouxel J 1980 *Physica* B **99** 3
[40] Su C Y, Lindau I, Chye P W, Oh S J and Spicer W E 1984 *J. Electron Spectrosc. Relat. Phenom.* B **30** 6251
[41] Wertheim G K and Buchanan D N E 1991 *Phys. Rev.* B **43** 13 815
[42] Kennou S, Ladas S and Papageorgopoulos C 1985 *Surf. Sci.* **152/153** 1213
[43] Brauer H E, Starnberg H I and Hughes H P to be published
[44] Wertheim G K and Hüfner S 1975 *Phys. Rev. Lett.* **35** 53
[45] Nozieres P and De Dominics C T 1969 *Phys. Rev.* **178** 1097
[46] Doniach S and Sunjic M 1970 *J. Phys. C: Solid State Phys.* **3** 285
[47] Wertheim G K and Walker L R 1976 *J. Phys. F: Met. Phys.* **6** 2297
[48] Scarfe J A and Hughes H P 1989 *J. Phys.: Condens. Matter* **1** 6865

[49] Ranke W and Kuhr H J 1989 *Phys. Rev.* B **39** 1595
[50] Jupille J, Dolle P and Besancon M 1992 *Surf. Sci.* **260** 271
[51] Shi H and Jacobi K 1992 *Surf. Sci.* **276** 12
[52] Shi H, Jacobi K and Ertl G 1992 *Surf. Sci.* **269/270** 682